Desalination and Water Treatment
www.deswater.com

doi: 10.5004/dwt.2022.28803

271 (2022) 307–316
September

Enhanced photocatalytic degradation of tetracycline over carbon quantum dot-decorated MIL-101(Fe) composite

Kun Bian, Fang-yan Chen*, Chen-chen Hao, Yu-bin Tang

School of Environmental and Chemical Engineering, Jiangsu University of Science and Technology, Zhenjiang 212100, China, Tel.: 86-511-85605157; email: chenfangyan@just.edu.cn (F.-y. Chen), Tel.: 86-511-85605156; email: 1070914202@qq.com (K. Bian), Tel.: 86-511-85605156; email: 1050948643@qq.com (C.-c. Hao), Tel.: 86-511-84448601; email: ybbill@163.com (Y.-b. Tang)

Received 5 April 2022; Accepted 3 August 2022

ABSTRACT

Carbon quantum dots (CQDs) were deposited on the surface of MIL101(Fe) by using hydrothermal method to obtain CQDs/MIL101(Fe) composite. The prepared composite was characterized by X-ray diffusion (XRD) spectroscopy, Fourier transform infrared (FT-IR) spectroscopy, scanning electron microscopy (SEM), transmission electron microscopy (TEM) and UV-Vis diffuse reflection spectrum. The photocatalytic performance of CQDs/MIL101(Fe) composite was evaluated by photocatalytic degradation of tetracycline (TC) under visible-light irradiation. The mechanism of enhanced photocatalytic performance was discussed. The characterization results reveal that CQDs is anchored tightly on the surface of MIL101(Fe) to form the composite catalyst. The results of photocatalytic degradation experiment confirm that CQDs/MIL101(Fe) possess excellent photocatalytic activity and stability for TC degradation. The CM100 with optimum CQDs-to-MIL101(Fe) rate shows the highest photocatalytic activity with TC degradation efficiency up to 81%. The reaction rate constant for CM100 is 0.01177 min^{-1}, which is 5.8 times as high as that of pure MIL101(Fe). The results of transient photocurrent response and electrochemical impedance indicate that the improvement of photocatalytic performance of the CQDs/MIL101(Fe) composites is mainly due to the introduction of CQDs, which greatly promotes the separation of photo-generated electron-hole pairs. The result of radical trapping experiment confirms that superoxide radical is the main active species in photocatalytic reaction, followed by photo-generated holes.

Keywords: Carbon quantum dots; MIL101(Fe); Photocatalyst; Tetracycline; Photocatalytic mechanism

1. Introduction

Tetracycline (TC) is an important antibiotic, which has been widely used in the treatment of human and animal infection [1]. However, owing to abuse of tetracycline, the drug residues have been entered the environment through various ways. Up to now, antibiotics and their metabolites have been detected in surface water, groundwater and drinking water [1,2], which will lead to increasing antibiotic resistance of potential bacteria and consequent threat to human health [3]. In order to solve these problems, a variety of strategies, such as adsorption [4,5], microbial degradation [6], membrane separation [7], electrochemical oxidation [8], piezocatalysis [9–13], and photocatalytic oxidation [14] have been developed to remove antibiotics from environment or wastewater. Among these methods, photocatalysis technology is to stimulate semiconductors to generate photoinduced charges through light energy and then photoproduced charges react with H_2O and O_2 in solution to produce $^{\bullet}O_2^-$, $^{\bullet}OH$ and other active species for the degradation of pollutants [15]. It is considered as a desirable method for degradation of organic pollutants due to its

* Corresponding author.

low cost, high efficiency, no secondary pollution [16–20]. Of course, designing and synthesizing a stable and efficient photocatalyst is the core of photocatalytic degradation of organic pollutants (such as TC) in water.

Metal organic frameworks (MOFs) have large specific surface area, high porosity and adjustable pore structure, so they are widely applied in catalytic synthesis [21], adsorption [22], drug delivery [23], gas separation and capture [24,25], chemical sensing [26], photocatalysis [27], and so on. In recent years, the research on photocatalytic degradation of organic pollutants by using MOFs as photocatalyst has attracted extensive interests [28–31]. Among many MOFs, Fe based MOFs (Fe-MOFs) has the advantages of visible-light response, high thermal stability, good hydrophobicity, low cost and non-toxicity. MIL101(Fe) is a typical Fe-MOFs. Its photogenerated electrons can transfer from highest occupied molecular orbital (HOMO) (oxygen orbit) to lowest unoccupied molecular orbit (LUMO) (metal cluster) under visible-light irradiation. It is regarded to be a visible-light-driven photocatalyst with promising application [32,33]. However, the rapid recombination of photo-generated electron-hole pairs in MIL101(Fe) seriously inhibits its photocatalytic activity [34,35]. Aiming at this shortcoming of MIL101(Fe), the introduction of cocatalyst is a common modification method [35–39]. Compared with metal cocatalysts, the cost of carbon materials as cocatalysts is lower, and the catalytic effect is significantly improved [40–42].

Carbon quantum dots (CQDs), a new type of nanocarbon materials, has been received extensive attention and used as cocatalysts because of its unique performance such as excellent light harvesting, adjustable photoluminescence and rapid electron transfer ability [43]. As a cocatalyst, CQDs can play a variety of roles. On the one hand, CQDs, as an electron storage and transmission medium, contributes to the migration and separation of photo-generated carriers [44]; On the other hand, it can increase the light absorption range and the reactive sites [45]. At present, some photocatalysts such as g-C_3N_4, MIL-125(Ti), etc. have been modified with CQDs as cocatalyst, and the results all prove that CQDs can effectively improve the photocatalytic performance of catalysts [46,47]. Regretfully, there are few reports on the modification of Fe-based MIL101(Fe) with CQDs for TC degradation.

In the present work, we first report CQDs/MIL101(Fe) composite prepared by one-step hydrothermal method in which the CQDs solution was directly added into the precursors of MIL101(Fe), not requiring CQDs particles to be prepared previously. The preparation process is facile and time-saving. The existence of CQDs effectively promotes the separation and migration of electron-holes pairs. The as-prepared CQDs/MIL101(Fe) exhibits significantly enhanced photocatalytic activity for removal of TC under visible-light irradiation. This work provided an idea for preparing high-efficient and stable MOF-based composite catalysts.

2. Material and methods

2.1. Materials

Citric acid, urea, terephthalic acid, ferric chloride hexahydrate, N,N-dimethylformamide, Ascorbic acid, 2-propanol and disodium ethylenediamine tetra-acetic acid are all in analytic grade and was purchased from Sinopharm Chemical Reagent Co., Ltd., (Shanghai, China).

2.2. Preparation of CQDs/MIL101(Fe)

The synthetic route of CQDs/MIL101(Fe) is shown in Fig. 1. Firstly, CQDs solution was prepared refers to the method reported in literature [44]. In brief, citric acid (5 g) and urea (1 g) were added into 25 mL of ultrapure water and stirred to be dissolved fully. Then the mixture was transferred into a 50 mL autoclave and heated at 180°C for 5 h in an oven. After reaction, the dark brown product was centrifuged at 8,000 rad/min for 5 min to remove large particles, and the CQDs solution was obtained. Subsequently, terephthalic acid (0.412 g) and $FeCl_3{\cdot}6H_2O$ (1.35 g) was added into 30 mL of N,N-dimethylformamide and stirred magnetically for 30 min. A certain amount of as-prepared CQDs solution was added to above solution and stirred for 30 min. Then the mixture was transferred into an autoclave and heated at 110°C for 20 h in an oven. After cooling to room temperature, the product was washed with deionized water and ethanol for several times, dried at 60°C for 12 h in a vacuum oven and ground to obtain CQDs/MIL101(Fe) composite. The CQDs/MIL101(Fe) with different CQDs contents, prepared by adding 25, 50, 100 and 150 μL of carbon quantum dot solutions, are designated as CM25, CM50, CM100 and CM150, respectively.

For comparison, MIL101(Fe) was synthesized with the same method as CQDs/MIL101(Fe) composite without the addition of CQDs solution.

2.3. Characterization of the photocatalyst

The crystal phase was detected by Empyrean X-ray diffractometer with Cu and Ka as radiation sources at a scanning speed of 7°/min. The morphology and micro structure of the samples were observed by a FEI-quanta 200 scanning electron microscope (SEM) and a FEI-Tecnai F20 transmission electron microscope (TEM). The element composition of the samples was determined by energy dispersive spectrometer (EDS). The infrared spectra of the samples were recorded by Cary 630 Fourier transform infrared (FT-IR) spectrometer. Raman spectra were performed on an LabRAM HR Evolution Raman spectrometer with a 532 nm He-Ne laser

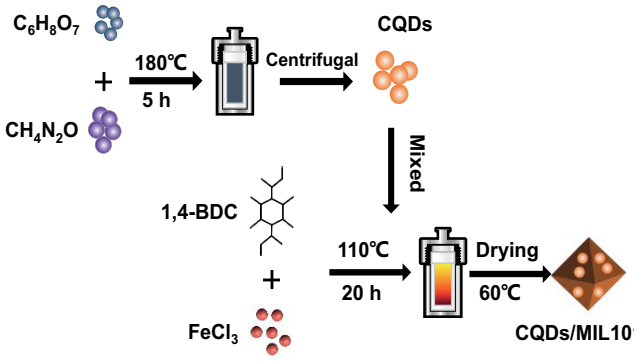

Fig. 1. Schematic illustration of CQDs/MIL101(Fe) synthesis process.

for excitation. The photoluminescence (PL) spectra of the samples were measured at the excitation wavelength of 446 nm with a RF-530IPC photoluminescence spectrometer. UV-vis spectra were recorded by an FTS-165 UV-vis spectrophotometer with $BaSO_4$ as the reference. CHIQ660D electrochemical workstation was used to test the electrochemical performance of the photocatalysts. Photocurrent and electrochemical impedance spectroscopy (EIS) were recorded by using an alternating voltage of 5 mV amplitude in the frequency range of 105 Hz to 10−2 Hz in 0.5 M Na_2SO_4 solution.

2.4. Photocatalytic performance test

The photocatalytic performance of the prepared catalyst was evaluated by the photocatalytic degradation of tetracycline (TC) in water under visible-light irradiation. 300 W xenon lamp with 420 nm cut-off filter was used as the light source, and the schematic diagram of experimental device is shown in Fig. S1. In a typical test, 20 mg of photocatalysts was added to 100 mL of TC aqueous solution with the initial concentration of 10 mg/L and initial pH of 6.8, stirred in the darkness for 30 min to ensure that the adsorption/desorption equilibrium was reached, then the TC solution was exposed to xenon lamp and stirred at a speed of 500 rpm for photocatalytic reaction. At 20 min intervals, 4 mL suspension were taken out and centrifuged to remove the photocatalysts. The concentration of TC was measured by a UV-vis spectrophotometer at the wavelength of 357 nm. The degradation efficiency of TC was calculated according to Eq. (1).

$$\text{Degradation rate}(\%) = 1 - \left(\frac{C}{C_0}\right) \times 100\% \quad (1)$$

where C represents the concentration of TC at a certain reaction time, and C_0 is the initial concentration of TC.

2.5. Cycle experiment of photocatalysts

The test procedure of photocatalytic reaction in cycle experiment are the same as that in Section 2.4 – Photocatalytic performance test. After the first photocatalytic reaction, photocatalysts were collected by centrifugation, washed with deionized water and absolute ethanol alternately, then dried at 60°C for the next reuse.

2.6. Active species capture experiment

Ascorbic acid (VC), 2-propanol (IPA) and disodium ethylenediamine tetra-acetic acid (EDTA-2Na) were added to TC solution to capture superoxide radical ($^{\bullet}O_2^-$), hydroxyl radical ($^{\bullet}OH$) and photo-induced hole (h^+), respectively. The concentration of capture agent is 1.0 mmol/L. In the presence of scavengers, the photocatalytic degradation of TC was conducted with the same method as that in Section 2.4.

3. Results and discussion

3.1. Characterization

The XRD patterns of CQDs/MIL101(Fe) are shown in Fig. 2a. In XRD pattern of the prepared MIL101(Fe), diffraction peaks at 2θ = 8.4°, 8.9°, 16.6° and 18.9° match well with the simulated XRD pattern of MIL101(Fe) reported in the literature [38], which indicates that the MIL101(Fe) in pure phase was successfully synthesized. Compared to pure MIL101(Fe), the XRD diffraction peaks of CM50 and CM100 remains unchanged. However, the peaks intensity of CM50 and CM100 become weaker than that of pure MIL101(Fe), suggesting the decreased periodicity of crystal lattice in MIL101(Fe). This may be due to the CQDs covering the surface of MIL101(Fe), which leads to the periodic reduction of its crystal lattice [45].

Fig. 2b gives the FT-IR spectrum of MIL101(Fe) and as-prepared composites. In FT-IR spectrum of MIL101(Fe), the peak appeared at 750 cm^{-1} is attributed to the C–H bond in benzene ring. The peaks at 1,020; 1,396 and 1,583 cm^{-1} correspond to carboxyl bond. The peak at 1,680 cm^{-1} originates from C=O in the carboxyl group [42]. The broad and weak peak at 3,420 cm^{-1} is assigned to the stretching vibration of –OH adsorbed on MIL101(Fe), which agree with previous report [48]. Compared with MIL101(Fe), the absorption peaks of CQDs/MIL101(Fe) at 750; 1,020; 1,396 and 1,583 cm^{-1} exhibit no variation. Whereas the absorption

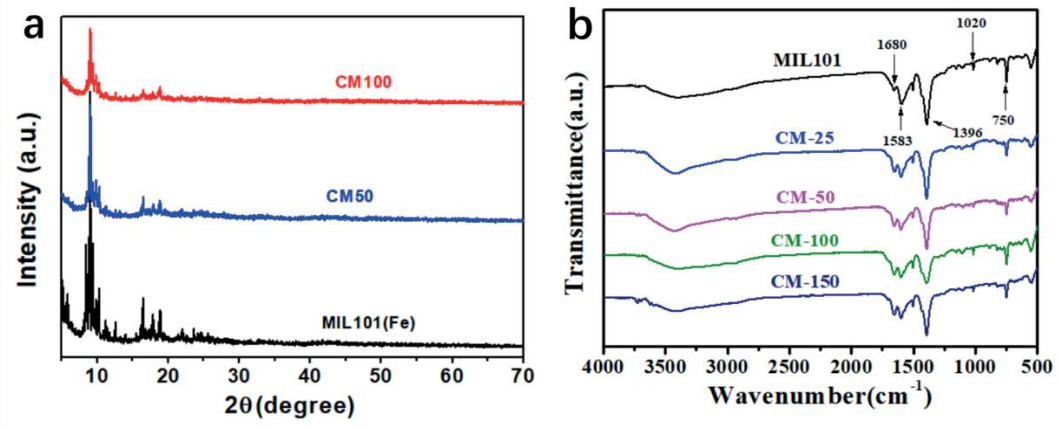

Fig. 2. (a) XRD patterns and (b) FT-IR spectra of MIL101(Fe) and CQDs/MIL101(Fe).

peak at 3,420 cm^{-1} become slightly intensified, indicating the existence of –OH from CQDs located on the surface of MIL101(Fe). The Raman spectra of CM100 was also measured and shown in Fig. S2. Two prominent peaks at 1,446 and 1,612 cm^{-1} can be clearly observed and corresponded to G band and D band of carbon, respectively [44,45], which further proves the existence of CQDs.

The morphologies of MIL101(Fe) and CQDs/MIL101(Fe) were observed by SEM and TEM. As can be seen from Fig. 3a, MIL101(Fe) presents an octahedron with average particle size of about 500 nm. Fig. 3b shows that CQDs/MIL101(Fe) exhibits similar shape with pure CQDs/MIL101(Fe), suggesting that the introduction of CQDs did not change the morphology of MIL101(Fe). It can be clearly found from TEM image of CQDs/MIL101(Fe) (Fig. 3c) that the surface of MIL101(Fe) is wrapped with CQDs nanoparticles, indicating that the CQDs are successfully anchored on the surface of MIL101(Fe). In the HRTEM image of CQDs/MIL101(Fe) (Fig. 3d), lattice stripes of CQDs with spacing of 0.256 nm can be observed [44], which further confirms that CQDs have been loaded on the surface of MIL101(Fe).

3.2. Photocatalytic performance

The photocatalytic performance of the prepared samples was evaluated by photodegradation of TC. As presented in Fig. 4a, MIL101(Fe) has good adsorption but poor photocatalytic effect toward TC. Within 120 min, the removal efficiency of TC is 44.7%. Compared with MIL101(Fe), CQDs/MIL101(Fe) shows decreased adsorption efficiency to TC, which may be because the loading of CQDs reduced the specific surface area of MIL101(Fe) to some extent. However, the degradation efficiency of TC under photocatalysis of CQDs/MIL101(Fe) was substantially improved. Among the three composites prepared by introducing various amount of CQDs solution, CM100 composite exhibits optimal photocatalytic activity with TC degradation efficiency of 81%, which is because CQDs can promote the separation of photogenerated electron–hole pairs. This is confirmed by the results from the transient photoelectric response and electrochemical impedance (shown in Fig. 6). Nevertheless, introduction of excess CQDs leads to the decrease in photocatalytic activity of CQDs/MIL101(Fe), which is because superfluous CQDs prevent the light absorption and shield the active sites of CQDs/MIL101(Fe) [43]. To further testify the degradation of TC, the UV-Vis spectra of photocatalytic degradation of TC was shown in Fig. S3. Furthermore, the UV-Vis spectra of photocatalytic degradation of TC over CM100 was shown in Fig. S3. In addition, the effect of pH value on photocatalytic degradation of TC was investigated. As shown in Fig. S4, the CM100 photocatalyst exhibited

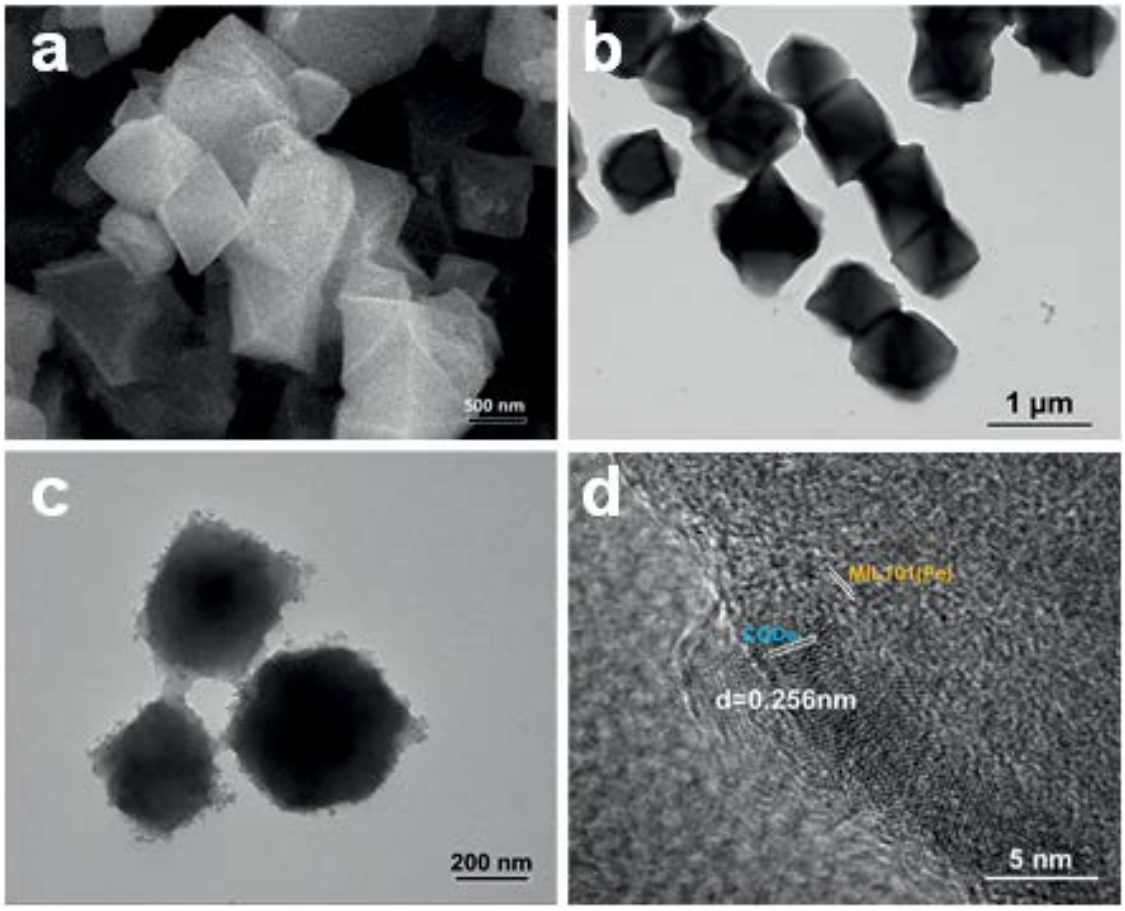

Fig. 3. SEM images of (a) MIL101(Fe) and (b) CM100; (c)TEM image of CM100 and (d) HRTEM image of CM100.

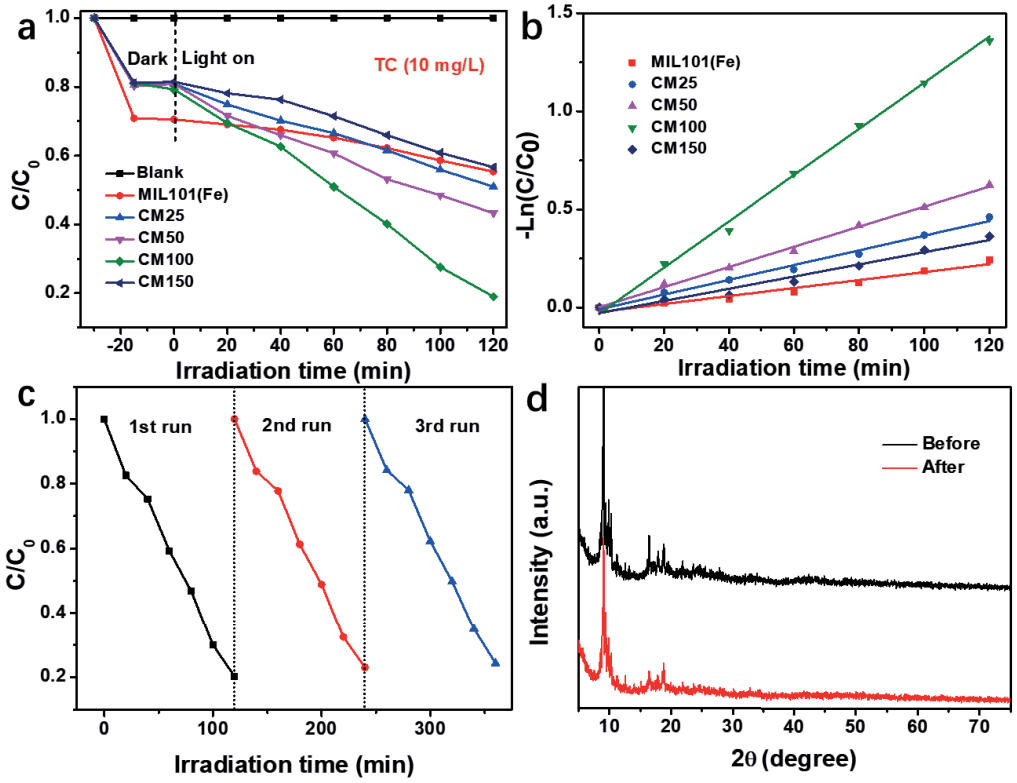

Fig. 4. (a) Photocatalytic degradation curve of TC (10 mg/L), (b) pseudo-first-order kinetic plots for TC photodegradation, (c) photocatalytic degradation of TC during three reuse of CM100 and (d) XRD pattern of CM100 before and after reuse.

excellent degradation efficiency for TC at pH range of 6.0–8.0. Under condition of pH ≤ 5.0 or pH ≥ 9.0, the degradation efficiency of TC was both low. This is perhaps because MIL-101(Fe) is not resistant to acid and alkali [49,50].

Generally, photocatalytic degradation rate of organic pollutant can be descripted by first-order reaction kinetic model shown in Eq. (2):

$$-\ln\left(\frac{C}{C_0}\right) = Kt \tag{2}$$

where K represents the degradation rate constant, and t is the illumination time.

Fig. 4b is the kinetic curve of TC degradation. According to the slope of kinetic curve, the degradation rate constant is calculated to be 0.00203, 0.00375, 0.00513, 0.01177 and 0.0031 min^{-1} for MIL101(Fe), CM25, CM50, CM100 and CM150, respectively. Evidently, the catalytic reaction rate constant for CM100 composite is the largest, which is 5.8 times as high as that of MIL101(Fe).

The stability of the prepared photocatalysts were judged by the cyclic utilization of CM100 for TC degradation. As depicted in Fig. 4c, after three rounds of reuse, the photocatalytic efficiency of CM100 for TC degradation remained at 75.8%, only reduced by 5%, which indicated that CM100 composite photocatalyst has excellent stability. Fig. 4b reveals that there is no significant change in the XRD pattern of CM100 before and after recycling. This indicates that the structure of the composite catalyst does not change during the photocatalytic reaction, which further confirmed the stability of CM100.

3.3. Optical properties and charge separation

The UV-Vis spectra of MIL101(Fe) and CQDs/MIL101(Fe) are given in Fig. 5. The absorption edge of CQDs/MIL101(Fe) slightly redshifts compared to MIL101(Fe). The band gap of semiconductor can be estimated by Tauc formula shown in Eq. (3) [51].

$$\alpha h\nu = A\left(h\nu - E_g\right)^{n/2} \tag{3}$$

where α is the light absorption coefficient, h is the Planck constant, v is the photon frequency, A is a constant, E_g is band gap and n is a constant that is depended on transition performance of the semiconductor. Because MIL101(Fe) is a direct semiconductor, n = 1. The Tauc plots of MIL101(Fe) and CQDs/MIL101(Fe) are shown in Fig. 5b. According to the slope of the curve in Fig. 5b, the band gap of CQDs/MIL101(Fe) are all 2.67 eV, which indicates that the incorporation of CQDs has no significant effect on the band gap of MIL101(Fe). Mott Schottky curve was determined to estimate the LUMO potential of CM100. As illustrated in Fig. 4c, the flat-band potential (Efb) of MIL101(Fe) is –0.78 V (vs. SCE), which is equivalent to –0.54 V (vs. NHE). Moreover, positive slope indicates that the composite has the characteristics similar with n-type semiconductor [52]. As for n-type semiconductor, ECB (or LUMO potential) is

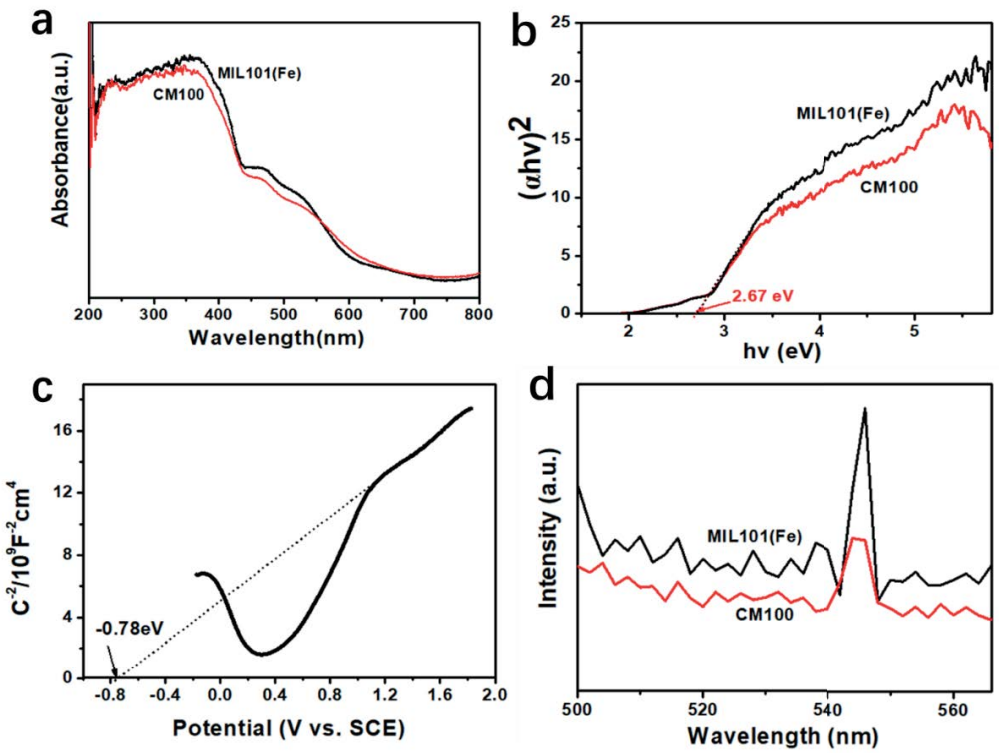

Fig. 5. (a) UV-vis spectra and (b) Tauc plots of MIL101(Fe) and CM100, (c) Mott-Schottky plots of CM100 and (d) PL spectra of MIL101(Fe) and CM100.

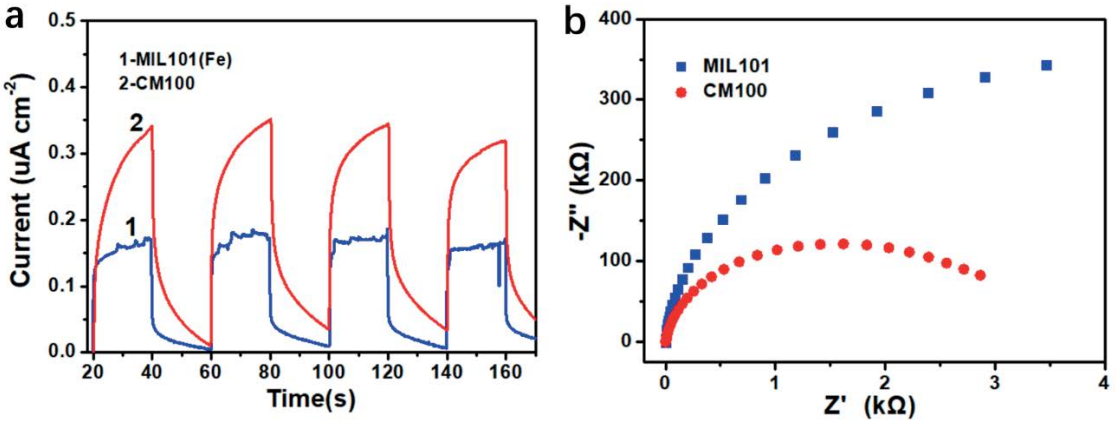

Fig. 6. (a) Photocurrent responses and (b) electrochemical impedance spectra of MIL101(Fe) and CM100.

approximately 0.10 V less than the Efb. Therefore, the LUMO potential of MIL101(Fe) is –0.64 eV. According to Eq. (4) [53], the HOMO potential of CM100 is calculated to be 1.99 eV.

$$E_g = E_{VB} - E_{CB} \quad (4)$$

Fig. 5d presents the PL spectra of MIL101(Fe) and CM100. The PL emission peaks of MIL101(Fe) and CM100 are all located at 540–550 nm. However, compared with MIL101(Fe), the emission peaks intensity of composite CM100 are obviously weakened. This means that CQDs loaded on the surface of MIL101(Fe) can effectively inhibit the recombination of electron–hole pairs [54].

In order to investigate the migration ability of the charge carriers for CQDs/MIL101(Fe), the transient photoelectric response and electrochemical impedance were conducted. As shown in Fig. 6a, CM100 exhibits significantly enhanced photocurrent intensity compared with MIL101(Fe), which verifies more efficient separation of photoinduced charge

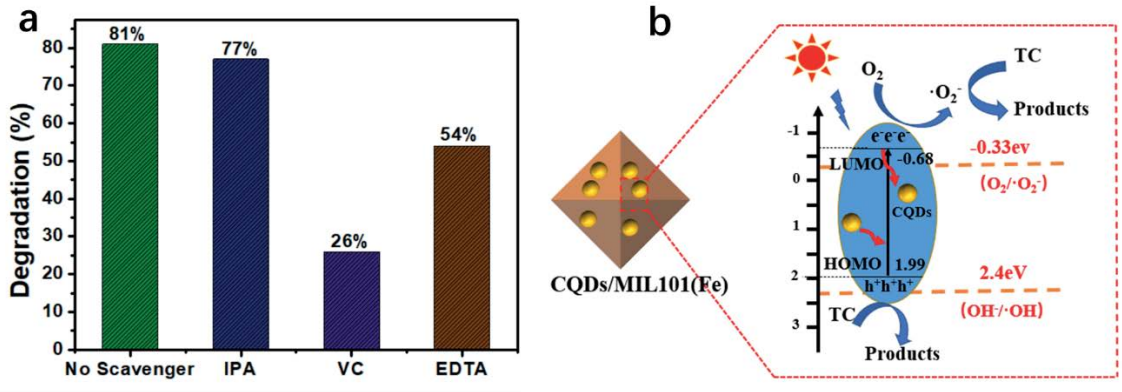

Fig. 7. (a) The results of active species trapping experiment for CM100 and (b) possible photocatalytic mechanism of CQDs/MIL101(Fe) for TC degradation.

carriers in CM100 [55]. Furthermore, the electrochemical impedance spectra (Fig. 6b) shows that the Nyquist arc radius of CM100 is considerably smaller than that of MIL101(Fe), meaning that the CM100 has lower resistance in electron migration, that is, more efficient separation for photoproduced charge carriers [56]. In a word, The CQDs anchored on the surface of MIL101(Fe) greatly boosts the separation of photogenerated electron-hole pairs, which results in enhanced photocatalytic activity of CM100.

3.4. Photocatalytic reaction mechanism

In order to expatiate the photocatalytic mechanism of CQDs/MIL101(Fe) for degradation of TC, the active species in photocatalytic reaction were identified by free radical trapping tests. Isopropanol (IPA), ascorbic acid (VC) and ethylenediamine tetraacetic acid (EDTA) were applied to capture hydroxyl radical (•OH), superoxide radical ($•O_2^-$) and photoinduced holes (h^+), respectively. As shown in Fig. 7a, the degradation efficiency of TC does not decrease obviously with the introduction of IPA, indicating that few •OH play a role in photocatalytic process. When VC and EDTA were added to TC solution, the photocatalytic efficiency decreased significantly from 81% to 26% and 54%, respectively, which confirms that the main active species in photocatalytic reaction is $•O_2^-$, followed by h^+.

Based on the trapping experimental result and CB and VB position, a possible photocatalytic mechanism of CQDs/MIL101(Fe) for TC degradation is proposed. As illustrated in Fig. 7b, owing to its narrow bandgap, MIL101(Fe) was excited under irradiation of visible-light to generate electrons and holes. Since CQDs acts as electron acceptors, the photogenerated electrons rapidly migrate from the LUMO of MIL101(Fe) to the surface of CQDs, which is conducive to inhibiting the recombination of the photoinduced electron-hole pairs. Since LUMO potential (–0.64 eV) of MIL101(Fe) is more negative than redox potential of $O_2/•O_2^-$ (–0.33 eV), the photoproduced electrons react with O2 to form plenty of $•O_2^-$, and the generated $•O_2^-$ oxidize TC. The holes remained in the HOMO of MIL101(Fe) directly participate in TC degradation to some extent. Nevertheless, •OH is difficult to be produced because the HOMO potential (1.99 eV) of MIL101(Fe) is more negative than the redox potential of $H_2O/•OH$ (2.4 eV), which has been verified by the result from radical trapping test.

4. Conclusions

The CQDs/MIL-101(Fe) was successfully synthesized by anchoring the CQDs on the surface of MIL101(Fe) via facile solvothermal method. In CQDs/MIL101(Fe) composite, CQDs function as local electron acceptor to effectively transfer photoinduced electrons from MIL101(Fe) and thus inhibits the recombination of the electron-hole pairs. CQDs/MIL101(Fe) exhibits dramatically enhanced photocatalytic activity in comparison with the pure MIL101(Fe). The photocatalytic activity is depended on content of CQDs in composite. The CM100, which was obtained by adding 100 μL CQDs solutions during preparation, shows the highest photocatalytic activity for TC degradation. Within 120 min, the removal of TC can reach up to 81%. Additionally, the result from radical trapping experimental testified that TC degradation is mainly attributed to superoxide radicals, followed by photoproduced holes.

Acknowledgements

This study is supported by Postgraduate Research & Practice Innovation Program of Jiangsu Province (KYCX21_3496).

References

[1] R. Daghrir, P. Drogui, Tetracycline antibiotics in the environment: a review, Environ. Chem. Lett., 11 (2013) 209–227.
[2] B.M. Marshall, S.B. Levy, Food animals and antimicrobials: impacts on human health, Clin. Microbiol. Rev., 24 (2011) 718–733.
[3] F. Baquero, J.-L. Martinez, R. Cantón, Antibiotics and antibiotic resistance in water environments, Curr. Opin. Biotechnol., 19 (2008) 260–265.
[4] X. Zhang, W. Guo, H.H. Ngo, H. Wen, N. Li, W. Wu, Performance evaluation of powdered activated carbon for removing 28 types of antibiotics from water, J. Environ. Manage., 172 (2016) 193–200.
[5] L.L. Yan, Y. Liu, Y. Zhang, S. Liu, C. Wang, W. Chen, C. Liu, Z. Chen, Y. Zhang, $ZnCl_2$ modified biochar derived from

aerobic granular sludge for developed microporosity and enhanced adsorption to tetracycline, Bioresour. Technol., 297 (2020) 122381, doi: 10.1016/j.biortech.2019.122381.
[6] Y.F. Leng, J.G. Bao, G.F. Chang, H. Zheng, X. Li, J. Du, D. Snow, X. Li, Biotransformation of tetracycline by a novel bacterial strain *Stenotrophomonas maltophilia* DT1, J. Hazard. Mater., 318 (2016) 125–133.
[7] A. Garcia-Rodríguez, V. Matamoros, S.D. Kolev, C.L. Font, Development of a polymer inclusion membrane (PIM) for the preconcentration of antibiotics in environmental water samples, J. Membr. Sci., 492 (2015) 32–39.
[8] Y. Liu, H. Liu, Z. Zhou, T. Wang, C.N. Ong, C.D. Vecitis, Degradation of the common aqueous antibiotic tetracycline using a carbon nanotube electrochemical filter, Environ. Sci. Technol., 49 (2015) 7974–7980.
[9] S. Zheng, X. Li, J. Zhang, J. Wang, C. Zhao, X. Hu, Y. Wu, Y. He, One-step preparation of MoO_x/ZnS/ZnO composite and its excellent performance in piezocatalytic degradation of Rhodamine B under ultrasonic vibration, J. Environ. Sci., 125 (2023) 1–13.
[10] X. Li, J. Wang, J. Zhang, C. Zhao, Y. Wu, Y. He, Cadmium sulfide modified zinc oxide heterojunction harvesting ultrasonic mechanical energy for efficient decomposition of dye wastewater, J. Colloid Interface Sci., 607 (2022) 412–422.
[11] L. Wang, J. Wang, C. Ye, K. Wang, C. Zhao, Y. Wu, Y. He, Photodeposition of CoO_x nanoparticles on $BiFeO_3$ nanodisk for efficiently piezocatalytic degradation of rhodamine B by utilizing ultrasonic vibration energy, Ultrason. Sonochem., 80 (2021) 105813, doi: 10.1016/j.ultsonch.2021.105813.
[12] Z. Li, Q. Zhang, L. Wang, J. Yang, Y. Wu, Y. He, Novel application of Ag/$PbBiO_2I$ nanocomposite in piezocatalytic degradation of rhodamine B via harvesting ultrasonic vibration energy, Ultrason. Sonochem., 78 (2021) 105729, doi: 10.1016/j.ultsonch.2021.105729.
[13] Y. Li, H. Chen, L. Wang, T. Wu, Y. Wu, Y. He, $KNbO_3$/ZnO heterojunction harvesting ultrasonic mechanical energy and solar energy to efficiently degrade methyl orange, Ultrason. Sonochem., 78 (2021) 105754, doi: 10.1016/j.ultsonch.2021.105754.
[14] K. Shu, F. Chen, W. Shi, F. Guo, Y. Tang, H. Ren, M. Li, Construction of $DyVO_4$/nitrogen deficient g-C_3N_4 composite for enhanced visible-light photocatalytic activity for tetracycline degradation, Mater. Res. Bull., 124 (2020) 110766–110774.
[15] X. Lu, Y. Wang, X. Zhang, G. Xu, D. Wang, J. Lv, Z. Zheng, Y. Wu, NiS and MoS_2 nanosheet co-modified graphitic C_3N_4 ternary heterostructure for highly efficient visible light photodegradation of antibiotic, J. Hazard. Mater., 341 (2018) 10–19.
[16] M.Y. Li, Y.B. Tang, W.L. Shi, F.Y. Chen, Y. Shi, H.C. Gu, Design of visible-light-response core-shell Fe_2O_3/$CuBi_2O_4$ heterojunctions with enhanced photocatalytic activity towards the degradation of tetracycline: Z-scheme photocatalytic mechanism insight, Inorg. Chem. Front., 5 (2018) 3148–3154.
[17] C. Liu, Y.B. Tang, P.W. Huo, F.Y. Chen, Novel AgCl/CNTs/g-C_3N_4 nanocomposite with high photocatalytic and antibacterial activity, Mater. Lett., 257 (2019) 126708–126711.
[18] H.J. Ren, Y.B. Tang, W.L. Shi, F.Y. Chen, Y.S. Xu, Red mud modified with graphene oxide for enhanced visible-light-driven photocatalytic performance towards the degradation of antibiotics, New J. Chem., 43 (2019) 19172–19179.
[19] C. Liu, F.Y. Chen, Y.B. Tang, P.W. Huo, An environmentally friendly nanocomposite polypyrrole@silver/reduced graphene oxide with high catalytic activity for bacteria and antibiotics, J. Mater. Sci.: Mater. Electron., 32 (2021) 15211–15225.
[20] C.C. Hao, Y.B. Tang, W.L. Shi, F.Y. Chen, F. Guo, Facile solvothermal synthesis of a Z-Scheme 0D/3D CeO_2/$ZnIn_2S_4$ heterojunction with enhanced photocatalytic performance under visible light irradiation, Chem. Eng. J., 409 (2021) 128168–128178.
[21] K. Shen, X.D. Chen, J.Y. Chen, Y.W. Li, Development of MOF-derived carbon-based nanomaterials for efficient catalysis, ACS Catal., 6 (2016) 5887–5903.
[22] Z. Ni, J.P. Jerrell, K.R. Cadwallader, R.I. Mase, Metal-organic frameworks as adsorbents for trapping and preconcentration of organic phosphonates, Anal. Chem., 79 (2007) 1290–1293.
[23] P. Horcajada, T. Chalati, C. Serre, B. Gillet, C. Sebrie, T. Baati, J.F. Eubank, D. Heurtaux, P. Clayette, C. Kreuz, J.S. Chang, Y.K. Hwang, V. Marsaud, P.N. Bories, L. Cynober, S. Gil, G. Ferey, P. Couvreur, R. Gref, Porous metal-organic framework nanoscale carriers as a potential platform for drug delivery and imaging, Nat. Mater., 9 (2010) 172–178.
[24] D. Alezi, Y. Belmabkhout, M. Suyetin, P.M. Bhatt, L.J. Weselinski, V. Solovyeva, K. Adil, I. Spanopoulos, P.N. Trikalitis, A.H. Emwas, M. Eddaoudi, MOF crystal chemistry paving the way to gas storage needs: aluminum-based soc-MOF for CH_4, O_2, and CO_2 storage, J. Am. Chem. Soc., 137 (2015) 13308–13318.
[25] X. Zhou, W.Y. Huang, J.P. Miao, Q.B. Xia, Z.J. Zhang, H.H. Wang, Enhanced separation performance of a novel composite material GrO@MIL-101 for CO_2/CH_4 binary mixture, Chem. Eng. J., 26 (2015) 6339–344.
[26] M. Wang, L. Guo, D.P. Cao, Metal-organic framework as luminescence turn-on sensor for selective detection of metal ions: absorbance caused enhancement mechanism, Sens. Actuators, B, 256 (2018) 839–845.
[27] D. Wang, F. Jia, H. Wang, F. Chen, Y. Fang, W. Dong, G. Zeng, X. Li, Q. Yang, X. Yuan, Simultaneously efficient adsorption and photocatalytic degradation of tetracycline by Fe-based MOFs, J. Colloid Interface Sci., 5 (2018) 273–284.
[28] J. Zhu, P.Z. Li, W. Guo, Y. Zhao, R. Zou, Titanium-based metal-organic frameworks for photocatalytic applications, Coord. Chem. Rev., 359 (2018) 80–101.
[29] A. Dhakshinamoorthy, Z. Li, H. Garcia, Catalysis and photocatalysis by metal organic frameworks, Chem. Soc. Rev., 47 (2018) 8134–8172.
[30] W. Huang, C. Jing, X. Zhang, M. Tang, L. Tang, M. Wu, N. Liu, Integration of plasmonic effect into spindle-shaped MIL-88A(Fe): steering charge flow for enhanced visible-light photocatalytic degradation of ibuprofen, Chem. Eng. J., 349 (2018) 603–612.
[31] X. Zhang, N. Yuan, Y. Li, L. Han, Q. Wang, Fabrication of new MIL-53(Fe)@TiO_2 visible-light responsive adsorptive photocatalysts for efficient elimination of tetracycline, Chem. Eng. J., 428 (2021) 131077–131090.
[32] D. Wang, F. Jia, H. Wang, F. Chen, Y. Fang, W. Dong, G. Zeng, X. Li, Q. Yang, X. Yuan, Simultaneously efficient adsorption and photocatalytic degradation of tetracycline by Fe-based MOFs, J. Colloid Interface Sci., 519 (2018) 273–284.
[33] N.V. Maksimchuk, O.V. Zalomaeva, I.Y. Skobelev, K.A. Kovalenko, V.P. Fedin, O.A. Kholdeeva, Metal–organic frameworks of the MIL-101 family as heterogeneous single-site catalysts, Proc. R. Soc. A, 468 (2012) 2017–2034.
[34] C.C. Wang, X.D. Du, J. Li, X.X. Guo, P. Wang, J. Zhang, Photocatalytic Cr(VI) reduction in metal-organic frameworks: a mini-review, Appl. Catal., B, 193 (2016) 198–216.
[35] C.C. Wang, X.H. Yi, P. Wang, Powerful combination of MOFs and C_3N_4 for enhanced photocatalytic performance, Appl. Catal., B, 247 (2019) 24–48.
[36] F.Y. Chen, K. Bian, H.S. Li, Y.B. Tang, C.C. Hao, W. Shi, A novel CeO_2/MIL101(Fe) heterojunction for enhanced photocatalytic degradation of tetracycline under visible-light irradiation, J. Chem. Technol. Biotechnol., 97 (2022) 1884–1892.
[37] L. He, Y. Zhang, Y. Zheng, Q. Jia, S. Shan, Y. Dong, Degradation of tetracycline by a novel MIL 101(Fe)/TiO_2 composite with persulfate, J. Porous Mater., 26 (2019) 1839–1850.
[38] Y. Gong, B. Yang, H. Zhang, X. Zhao, A g-C_3N_4/MIL-101(Fe) heterostructure composite for highly efficient BPA degradation with persulfate under visible light irradiation, J. Mater. Chem. A, 6 (2018) 23703–23711.
[39] J. Huang, H. Song, C. Chen, Y. Yang, N. Xu, X. Ji, C. Li, J.A. You, Facile synthesis of N-doped TiO_2 nanoparticles caged in MIL-100(Fe) for photocatalytic degradation of organic dyes under visible light irradiation, J. Environ. Chem. Eng., 5 (2017) 2579–2585.
[40] D. Yan, H. Hu, N. Gao, J. Ye, H. Ou, Fabrication of carbon nanotube functionalized MIL-101(Fe) for enhanced visible-light photocatalysis of ciprofloxacin in aqueous solution, Appl. Surf. Sci., 498 (2019) 143836–143844.

[41] N. Liu, M. Tang, J. Wu, L. Tang, L. Wang, Boosting visible-light photocatalytic performance for CO_2 reduction via hydroxylated graphene quantum dots sensitized MIL-101(Fe), Adv. Mater. Interfaces, 7 (2020) 2000468–2000478.
[42] J. Lin, H. Hu, N. Gao, J. Ye, Y. Chen, H. Ou, Fabrication of GO@MIL-101(Fe) for enhanced visible-light photocatalysis degradation of organophosphorus contaminant, J. Water Process Eng., 33 (2020) 101010–101018.
[43] F.Y. Chen, L. Cheng, Y.B. Tang, K.K. Shu, W.L. Shi, Construction of Z-scheme heterojunction g-C_3N_4/CQDs/$InVO_4$ with broad-spectrum response for efficient rhodamine B degradation and H_2 evolution under visible light, J. Chem. Technol. Biotechnol., 96 (2021) 3074–3083.
[44] Y. Liu, C. Liu, C. Shi, W. Sun, X. Lin, W. Shi, Y. Hong, Carbon-based quantum dots (CQDs) modified *ms*/*tz*-$BiVO_4$ heterojunction with enhanced photocatalytic performance for water purification, J. Alloys Compd., 881 (2021) 160437, doi: 10.1016/j.jallcom.2021.160437.
[45] W. Sun, S. Yang, Y. Liu, C. Shi, W. Shi, X. Lin, F. Guo, Y. Hong, Fabricating nitrogen-doped carbon dots (NCDs) on $Bi_{3.64}Mo_{0.36}O_{6.55}$ nanospheres: a nanoheterostructure for enhanced photocatalytic performance for water purification, J. Phys. Chem. Solids, 159 (2021) 110283, doi: 10.1016/j.jpcs.2021.110283.
[46] W. Shi, W. Sun, Y. Liu, X. Li, X. Lin, F. Guo, Y. Hong, Onion-ring-like g-C_3N_4 modified with Bi_3TaO_7 quantum dots: a novel 0D/3D S-scheme heterojunction for enhanced photocatalytic hydrogen production under visible light irradiation, Renewable Energy, 182 (2022) 958–968.
[47] Z. Li, G. Che, W. Jiang, L. Liu, H. Wang, Visible-light-driven CQDs@MIL-125(Ti) nanocomposite photocatalyst with enhanced photocatalytic activity for the degradation of tetracycline, RSC Adv., 9 (2019) 33238–33245.
[48] L. He, Y. Dong, Y. Zheng, Q. Jia, S. Shan, Y. Zhang, A novel magnetic MIL-101(Fe)/TiO2 composite for photo degradation of tetracycline under solar light, J. Hazard. Mater., 361 (2019) 85–94.
[49] C. Wang, X. Liu, N. Keser Demir, J.P. Chen, K. Li, Applications of water stable metal–organic frameworks, Chem. Soc. Rev., 45 (2016) 5107–5134.
[50] D. Pattappan, S. Vargheese, K.V. Kavya, R.T. Rajendra Kumar, Y. Haldorai, Metal-organic frameworks with different oxidation states of metal nodes and aminoterephthalic acid ligand for degradation of Rhodamine B under solar light, Chemosphere, 286 (2022) 131726, doi: 10.1016/j.chemosphere.2021.131726.
[51] F.Y. Chen, X. Zhang, Y.B. Tang, X.G. Wang, K.K. Shu, Facile and rapid synthesis of a novel spindle-like heterojunction $BiVO_4$ showing enhanced visible-light-driven photoactivity, RSC Adv., 10 (2020) 5234–5240.
[52] L. Cheng, F.Y. Chen, Z.Q. Zhu, Y.B. Tang, K.K. Shu, W.L. Shi, Vacancy-modified g-C_3N_4 nanosheets via one-step thermal polymerization of thiosemicarbazide precursor for visible-light-driven photocatalytic activity, Mater. Chem. Phys., 275 (2022) 125192–125202.
[53] X. Zhang, F.Y. Chen, Y.B. Tang, Y.M. Liu, X.G. Wang, A rapid microwave synthesis of nanoscale $BiVO_4$/Bi_2O_3@SiO_2 with large specific surface area and excellent visible-light-driven activity, Desal. Water Treat., 152 (2019) 99–107.
[54] F.Y. Chen, M.K. He, Y.B. Tang, C.Y. He, K.K. Shu, M.Y. Li, A facile vapor deposition synthesis of g-C_3N_4/SiO_2 nanocomposite with large specific surface area and enhanced photocatalytic activity, Desal. Water Treat., 196 (2020) 247–255.
[55] N. Liu, W. Huang, M. Tang, C. Yin, B. Gao, Z. Li, L. Tang, J. Lei, L. Cui, X. Zhang, In-situ fabrication of needle-shaped MIL-53(Fe) with 1T-MoS_2 and study on its enhanced photocatalytic mechanism of ibuprofen, Chem. Eng. J., 359 (2019) 254–264.
[56] J. Low, L. Zhang, T. Tong, L. Wu, J. Lu, TiO_2/MXene Ti_3C_2 composite with excellent photocatalytic CO_2 reduction activity, J. Catal., 361 (2018) 255–266.

Supplementary information:

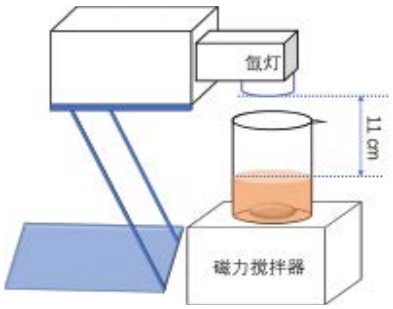

Fig. S1. The schematic diagram of photocatalytic reaction device.

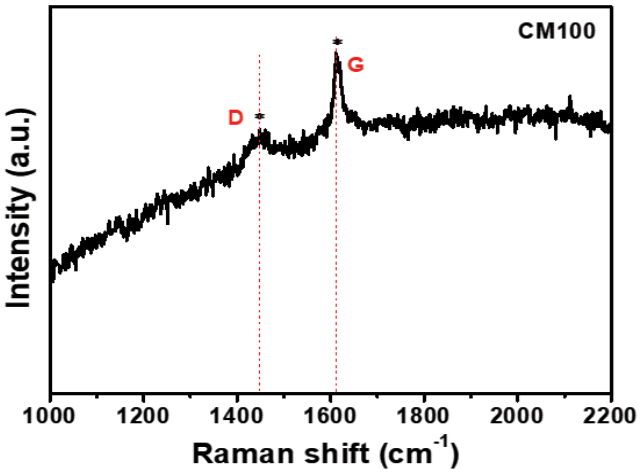

Fig. S2. The Raman spectra of CM100.

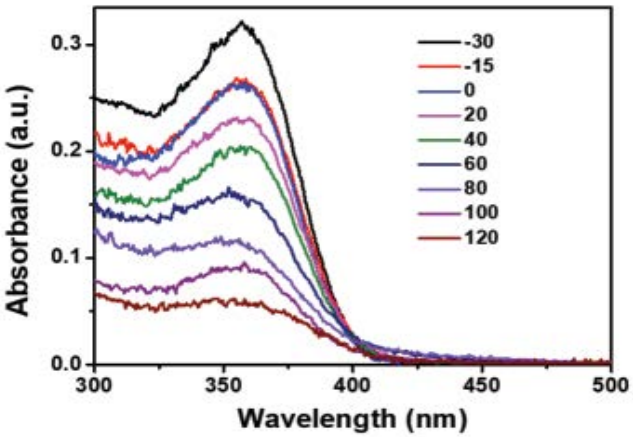

Fig. S3. UV-Vis spectra of photocatalytic degradation of TC over CM100.

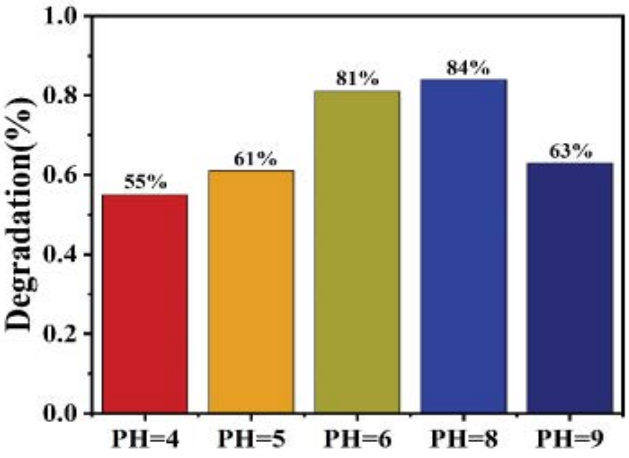

Fig. S4. Effect of pH on photocatalytic degradation of TC over CM100.